nature geoscience

Article

https://doi.org/10.1038/s41561-023-01125-2

Global patterns of water storage in the rooting zones of vegetation

Received: 8 October 2021

Accepted: 6 January 2023

Benjamin D. Stocker[1,2,3,4,5] ✉, **Shersingh Joseph Tumber-Dávila**[1,6], **Alexandra G. Konings**[1], **Martha C. Anderson**[7], **Christopher Hain**[8] & **Robert B. Jackson**[1,9,10]

The rooting-zone water-storage capacity—the amount of water accessible to plants—controls the sensitivity of land–atmosphere exchange of water and carbon during dry periods. How the rooting-zone water-storage capacity varies spatially is largely unknown and not directly observable. Here we estimate rooting-zone water-storage capacity globally from the relationship between remotely sensed vegetation activity, measured by combining evapotranspiration, sun-induced fluorescence and radiation estimates, and the cumulative water deficit calculated from daily time series of precipitation and evapotranspiration. Our findings indicate plant-available water stores that exceed the storage capacity of 2-m-deep soils across 37% of Earth's vegetated surface. We find that biome-level variations of rooting-zone water-storage capacities correlate with observed rooting-zone depth distributions and reflect the influence of hydroclimate, as measured by the magnitude of annual cumulative water-deficit extremes. Smaller-scale variations are linked to topography and land use. Our findings document large spatial variations in the effective root-zone water-storage capacity and illustrate a tight link among the climatology of water deficits, rooting depth of vegetation and its sensitivity to water stress.

To sustain activity during dry periods and resist impacts of droughts, plants rely on water stored below the surface. The larger the rooting-zone water-storage capacity (S_0), the longer plants can withstand soil moisture limitation[1]. S_0 is therefore a key factor determining drought impacts, land–atmosphere exchanges and run-off regimes, particularly in climates with a seasonal asynchrony in radiation and precipitation (P)[2–4]. In models, S_0 is commonly conceived as a function of the soil texture and the plants' rooting depth (z_r), limited to the depth of the soil[3,5]. Recent research has revealed a substantial component of S_0 and contributions to evapotranspiration (ET) by water stored beneath the soil, in weathered and fractured bedrock and groundwater[6–11]. Plant access to such deep moisture plays an important role in controlling near-surface climate[12–14], run-off regimes[4], global patterns of vegetation cover[15] and mitigating impacts of droughts[16].

However, S_0 is impossible to observe directly across large scales, and its spatial variations are poorly understood[17]. Global compilations of local plant z_r measurements[18,19] yield information related to S_0 but have resolved this observational challenge only partly because of their limited size and large documented variations in z_r across multiple scales[7,18,18–21]. Empirical approaches for estimating the global z_r distribution have made use of relationships between in situ observations and climatic factors[22]. Modelling approaches for predicting z_r have

[1]Department of Earth System Science, Stanford University, Stanford, CA, USA. [2]Department of Environmental Systems Science, ETH, Zürich, Switzerland. [3]Swiss Federal Institute for Forest, Snow and Landscape Research WSL, Birmensdorf, Switzerland. [4]Institute of Geography, University of Bern, Bern, Switzerland. [5]Oeschger Centre for Climate Change Research, University of Bern, Bern, Switzerland. [6]Harvard Forest, Harvard University, Petersham, MA, USA. [7]USDA-ARS Hydrology and Remote Sensing Laboratory, Beltsville, MD, USA. [8]NASA Marshall Space Flight Center, Redstone Arsenal, AL, USA. [9]Woods Institute for the Environment, Stanford University, Stanford, CA, USA. [10]Precourt Institute for Energy, Stanford University, Stanford, CA, USA. ✉e-mail: benjamin.stocker@giub.unibe.ch

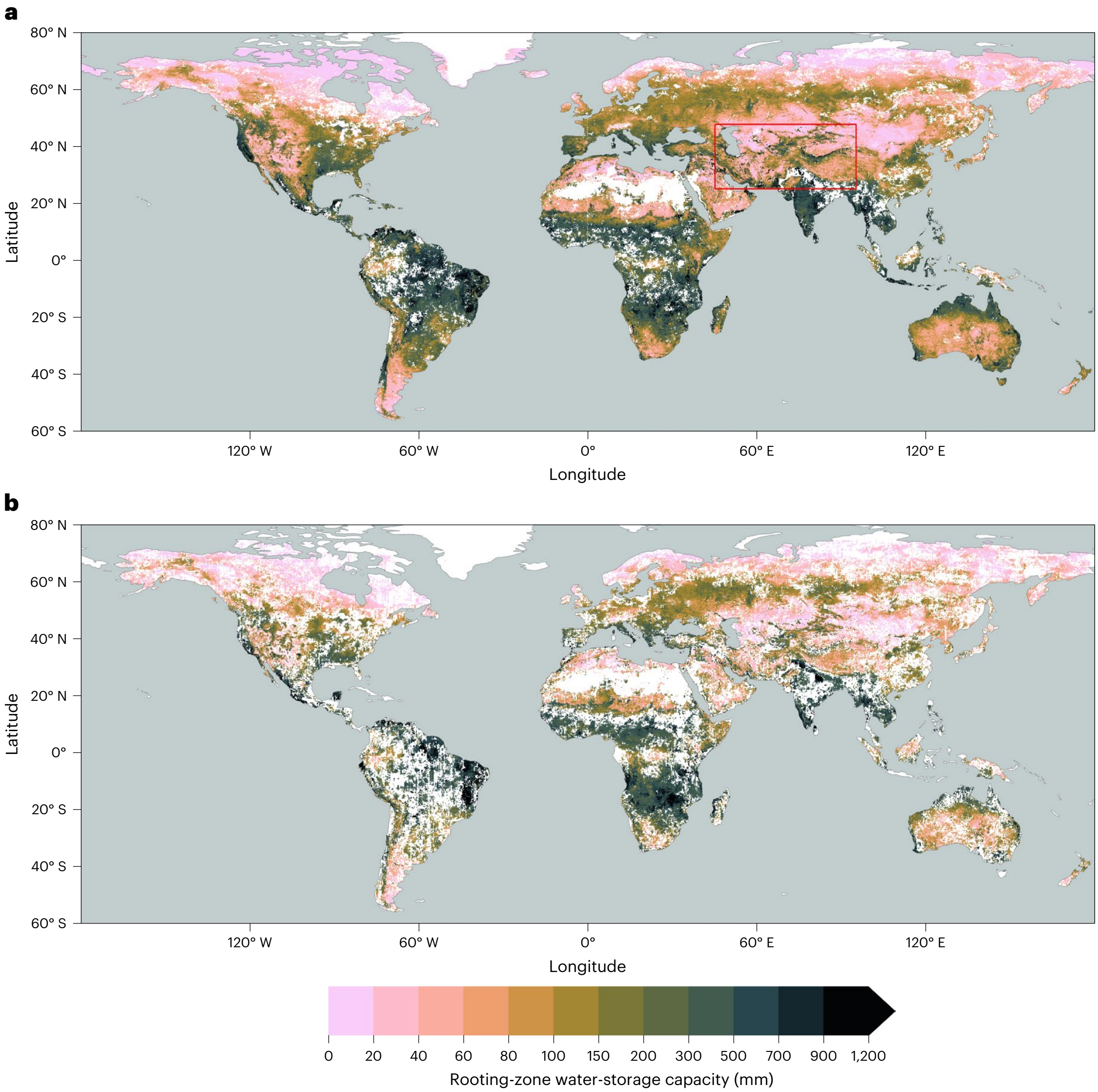

Fig. 1 | Rooting-zone water-storage capacity from vegetation activity. **a**,**b**, Rooting-zone water-storage capacity estimated from S_{dEF} (**a**) and S_{dSIF} (**b**) to the CWD. The red box in **a** shows the outline of the magnified map provided in Fig. 2. Data shown are aggregated to 0.1° resolution. Blank cells (white) mark areas where all underlying cells at the original 0.05° resolution did not exhibit a significant and single, linearly declining relationship with increasing CWD.

conceived their spatial variations as the result of optimal adaptation to the prevailing hydroclimate[23–25] or as being adapted to just buffer water demand to sustain ET during dry periods[2,26]. Such mass-balance approaches make use of the maximum cumulative water deficit (CWD) during dry periods as an indication of the effective S_0. An additional hypothesis posits that it would not be beneficial for plants to root even deeper and thus size their S_0 even larger[26]. However, a link among the magnitude of CWD extremes, the sensitivity of vegetation activity to an increasing CWD and local z_r observations remains to be shown, and the prevalence of plant access to water stored at depth (here taken as >2 m) across the globe remains to be quantified.

Despite its crucial role in controlling water and carbon fluxes and the scarcity of observations, virtually all models simulating water and carbon exchange between the land surface and the atmosphere rely on a specification of S_0 either directly as the depth of a 'water bucket' or indirectly through prescribed z_r and soil texture across the profile. Typically, water stored at depth and along the entire critical zone (including weathered bedrock) is not fully represented in models[8,9], and the evident plasticity of z_r and variations of S_0 within plant types and along climatic and topographic gradients are often ignored. Implications of this simplification may be substantial for the simulation of land–atmosphere coupling and drought impacts[8,12,13].

In this Article, we present a method for diagnosing S_0 from the relationship between vegetation activity and CWD. By fusing multiple time series of Earth observation data streams with global coverage, we estimate the global distribution of S_0 at a resolution of 0.05° (~5 km). Using a mass-balance approach[2,26] and field observations of z_r from a globally distributed dataset, we then show that the sensitivity of vegetation to water stress across the globe is strongly related to the magnitude of CWD extremes and reflects the rooting depth of plants.

Estimating S_0 from Earth observations

We started by estimating S_0 as the CWD at which vegetation 'activity' ceases. Our approach accounts for the constraint of the rooting-zone water availability on ET and photosynthesis and relates S_0 to the sensitivity of vegetation activity to water stress. The parallel information of

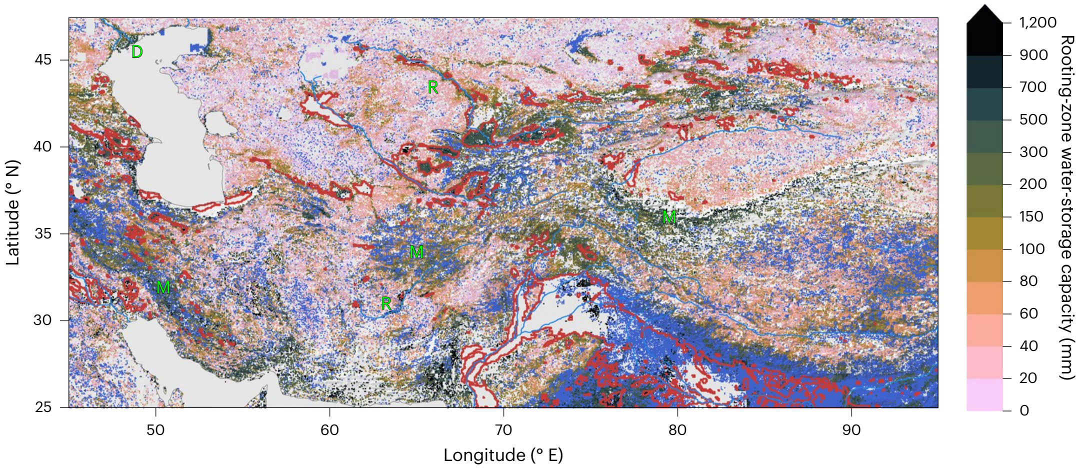

Fig. 2 | Rooting-zone water-storage capacity in Central Asia, estimated from S_{dEF}. Blue areas (flattening) show grid cells where a significant reduction in the slope in EF versus CWD was identified beyond a certain threshold. S_{dEF} values are not calculated for grid cells classified as flattening. Red lines outline major irrigated areas, where the irrigated land area fraction is above 30%[41]. Information about irrigated areas was used only for mapping here, but is not used for other parts of the analysis. Blank grid cells (white) indicate areas with a sustained imbalance of ET being greater than P. Green letters indicate locations of mountains (M), rivers (R) and delta (D), referred to in the main text. Additional regional maps are provided by Extended Data Figs. 1–3.

ET, P and the modelled snow mass balance enables a quantification of CWD over time. Vegetation activity was estimated from two alternative observations: from the evaporative fraction (EF, defined as ET divided by net radiation) and from sun-induced fluorescence (SIF, normalized by incident short-wave radiation (Methods)).

Figure 1 reveals large global variations in S_0. Estimates based on EF and SIF correlate closely and agree in magnitude ($R^2 = 0.78$; Supplementary Fig. 1). The lowest sensitivity of vegetation activity to an increasing CWD, and thus the largest apparent S_0, is found in regions with a strong seasonality in radiation and water availability and substantial vegetation cover—particularly in monsoonal climates. By contrast, the lowest S_0 values appear not only in regions where seasonal water deficits are limited due to short inter-storm duration (for example, western Amazon and Congo basin) and/or low levels of potential ET (for example, high latitudes), but also in deserts and arid grasslands. This probably reflects the limited water storage accumulating during rain events from which vegetation can draw during dry periods. In these regions, a rapid decline of ET and SIF with an increasing CWD is related to vegetation cover dynamics, governed by greening after rain pulses and browning during dry periods[27].

Clear patterns emerge also at smaller scales (Fig. 2 and Extended Data Figs. 1–3). The sensitivity of SIF (S_{dSIF}) and sensitivity of the EF (S_{dEF}) consistently (Supplementary Fig. 1) reveal how the sensitivity of photosynthesis and transpiration to drought stress varies across different topographical settings, indicating generally larger S_0 in mountain regions ('M' in Fig. 2) and along rivers ('R') and deltas ('D'). We note, however, that ET estimates from the product used here (ALEXI[28,29]) may be biased high over mountainous terrain where low incident net radiation and surface temperatures are caused not by high EFs but rather by topography effects and local shading. The maps of S_{dSIF} and S_{dEF} also bear strong imprints of human land use. Major irrigated cropland areas are congruent with some of the highest apparent S_0 values. In these areas, our analysis yields particularly high CWD values and a low sensitivity of SIF and EF to CWD, without using information about the location and magnitude of irrigation. Other major irrigated areas appear as blank cells in Fig. 2 because the algorithm used to calculate CWD (Methods) fails due to a long-term imbalance between P and ET and a 'runaway CWD'. This indicates sustained overuse of water resources, caused by lateral water redistribution at scales beyond ~5 km via streamflow diversion or groundwater flow and extraction (or bias in P and ET estimates).

Regressing vegetation activity against CWD also identifies locations where a decoupling of the two variables appears, that is, where the sensitivity of EF or SIF significantly decreases beyond a certain CWD threshold ('flattening' in Fig. 2; Methods). Such areas are particularly common in the vicinity of mountain regions, in areas with irrigated croplands and in savannahs (Supplementary Fig. 2). Related mechanisms may be at play. A flattening of the EF (SIF) versus CWD relationship is probably due to different portions of the vegetation having access to distinct water resources and respective storage capacities. In areas with large topographic gradients, this may be due to within-grid-cell heterogeneity in plant access to the saturated zone. Although relevant for land–atmosphere coupling[12], land surface models typically do not account for such effects. This has potential implications for simulations of ET during prolonged dry periods in these regions. In savannahs, a shift in ET contributions from grasses and trees and a related shift in transpiration occurs as grasses, which are often more shallow rooted than trees[30], senesce. In irrigated cropland areas, the flattening probably reflects land-use heterogeneity within ~5 km grid cells and the persistent water access on irrigated fields while EF and SIF are reduced more rapidly in surrounding vegetation.

What controls spatial variations in S_0 and z_r and the sensitivity of vegetation activity to water stress? Following ref. [2], we hypothesized that annual CWD maxima reflect the total amount of plant-accessible water. That is, z_r and S_0 are sized to just maintain transpiration and photosynthesis under extreme water deficits, commonly experienced over the course of a plant's lifetime (recurring with a return period of T yr). Hence, a correlation between the magnitude of CWD extremes and the sensitivity of vegetation activity to an increasing CWD should emerge. For estimating CWD extremes, we started by using $T = 80$ yr and assessed other choices as described in Supplementary Text 1 (also see Extended Data Fig. 4).

Figure 3a shows the global distribution of S_{CWDX80} and reveals patterns across multiple scales—in close agreement with S_{dSIF} and S_{dEF} ($R^2 = 0.76$ and $R^2 = 0.83$, respectively; Supplementary Fig. 3). This indicates that the sensitivity of vegetation activity to an increasing CWD (measured by S_{dSIF} and S_{dEF}) is strongly controlled by hydroclimate (as measured by S_{CWDX80}). The agreement between S_0 estimates based on water mass-balance approaches[2,26] and vegetation activity suggests that plants tend to size their roots no deeper, and S_0 no larger, than what is suggested by observed CWD extremes. Magnitudes of S_{CWDX80} inferred for 55% (37%) of Earth's vegetated regions indicate plant access to

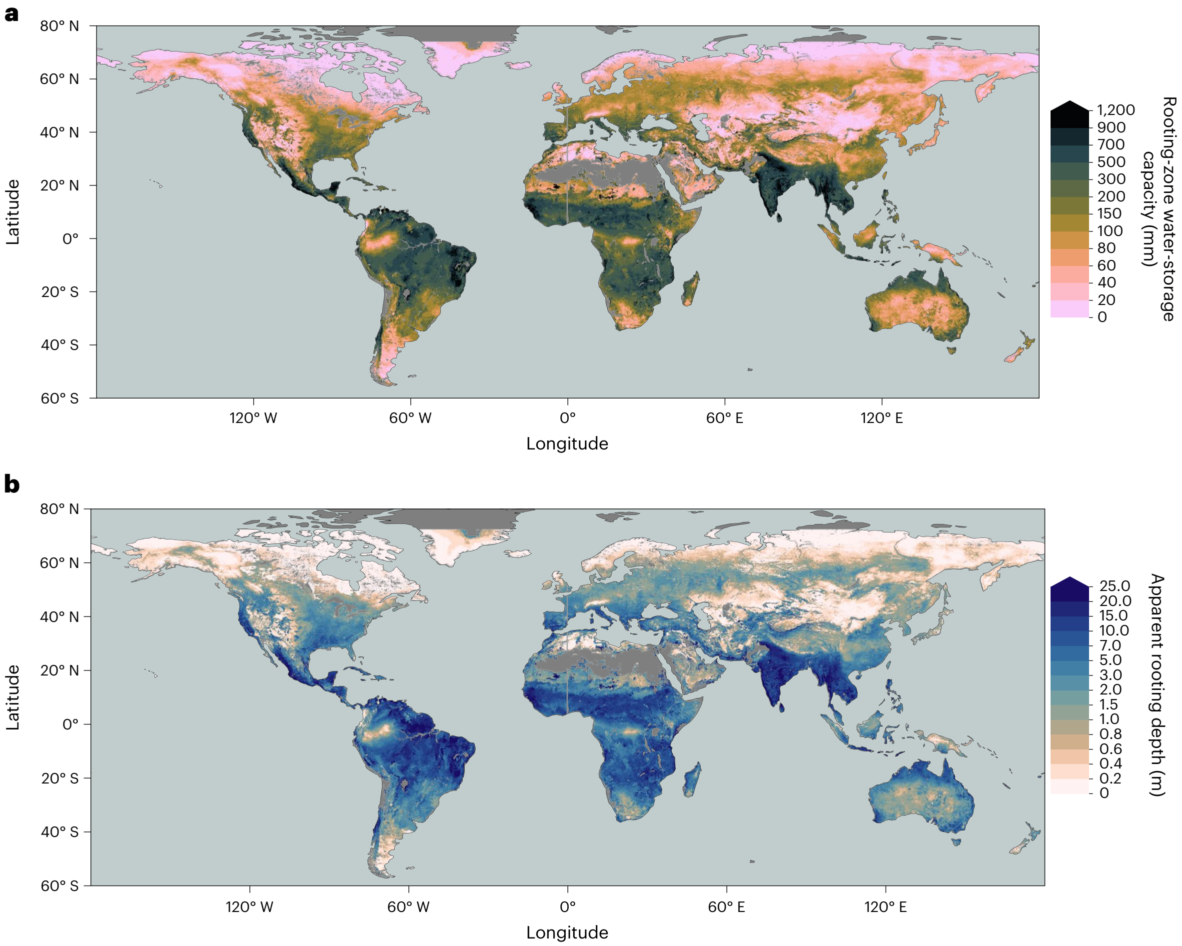

Fig. 3 | Rooting-zone water-storage capacity and apparent rooting depth from the water mass balance. a,**b**, Spatial variations of the rooting-zone water-storage capacity, estimated by S_{CWDX80} (**a**) and the apparent rooting depth z_{CWDX80} (**b**). Values are remapped to 0.1° resolution. Blank grid cells (grey) are either permanent inland water bodies and ocean or locations with long-term accumulation of water deficits. Values are removed in grid cells where more than 99% is non-vegetation surface according to MODIS Landcover[42].

water stored beyond 1 (2) m soil, assuming texture-dependent WHC[31–33] (Extended Data Figs. 5 and 6).

Fine granularity and large spatial heterogeneity of S_{CWDX80} at regional scales reveal the importance of land use and the local topographical setting for determining plant-available water-storage capacities (Extended Data Figs. 7 and 8). Complex patterns emerge. Mountainous areas feature higher S_{CWDX80} than their surrounding lowlands. In other regions, lowlands feature some of the highest recorded S_{CWDX80}. In these regions, irrigated agriculture is widespread (Fig. 2 and Extended Data Fig. 1). Variations are likely to extend to even smaller scales along the hillslope topography[7] and within individual forest stands[34]. These scales lie beyond the resolution of the satellite remote-sensing data used here to calculate CWD.

Evaluation with rooting-depth observations

The S_0 provides an estimate of the effective total plant-available water, independent of assumptions about physical constraint (limited soil depth, shallow bedrock or groundwater) and independent of uncertain soil texture and water-holding capacity (WHC). Due to the absence of direct observational constraints on S_0, we converted S_0 to a corresponding apparent z_r, enabling an evaluation of S_0 estimates against fully independent observations. We focused on comparing biome-level distributions of inferred apparent rooting depth (z_{CWDX80}) with a dataset[30] containing 5,524 individual field observations of plant rooting depth from 1,705 globally distributed sites (Supplementary Fig. 4). We thus tested the link between hydroclimate and below-ground vegetation structure across large climatic gradients.

Predicted and observed biome-level maximum rooting depth (90% quantiles) are correlated (Pearson's $r = 0.68$; Fig. 4c) while the lower (10%) quantiles appear to be overestimated by z_{CWDX80} (Fig. 4b). Using a subset of the data where information about the water-table depth (WTD) is provided (489 entries from 359 sites), we limited values of z_{CWDX80} to the value of the observed local WTD (53% of all observations). This yields a strongly improved correlation of observed and estimated biome-level 10% rooting-depth quantiles (Pearson's $r = 0.91$; Fig. 4d) compared with estimates that are not capped at the observed WTD (Fig. 4b). This suggests that inferred z_r overestimates values where roots access the groundwater and indicates that groundwater access is relevant across more than half of the globally distributed sites in our dataset. While acting as a constraint on the rooting depth[7], plant access to groundwater or a perched water table implies sustained transpiration during dry periods, correspondingly large CWDs and, by implication of the model design, large S_{CWDX80} and (apparent) z_{CWDX80}.

Influence of biotic and abiotic factors

Using first-principles modelling and integrating multiple data streams, we diagnosed a hydrologically effective ecosystem-level S_0 from the sensitivity of vegetation activity to CWD. We found that large-scale variations in S_0 are driven by the hydroclimate and that global patterns of seasonal water deficits are reflected in the rooting depth of plants.

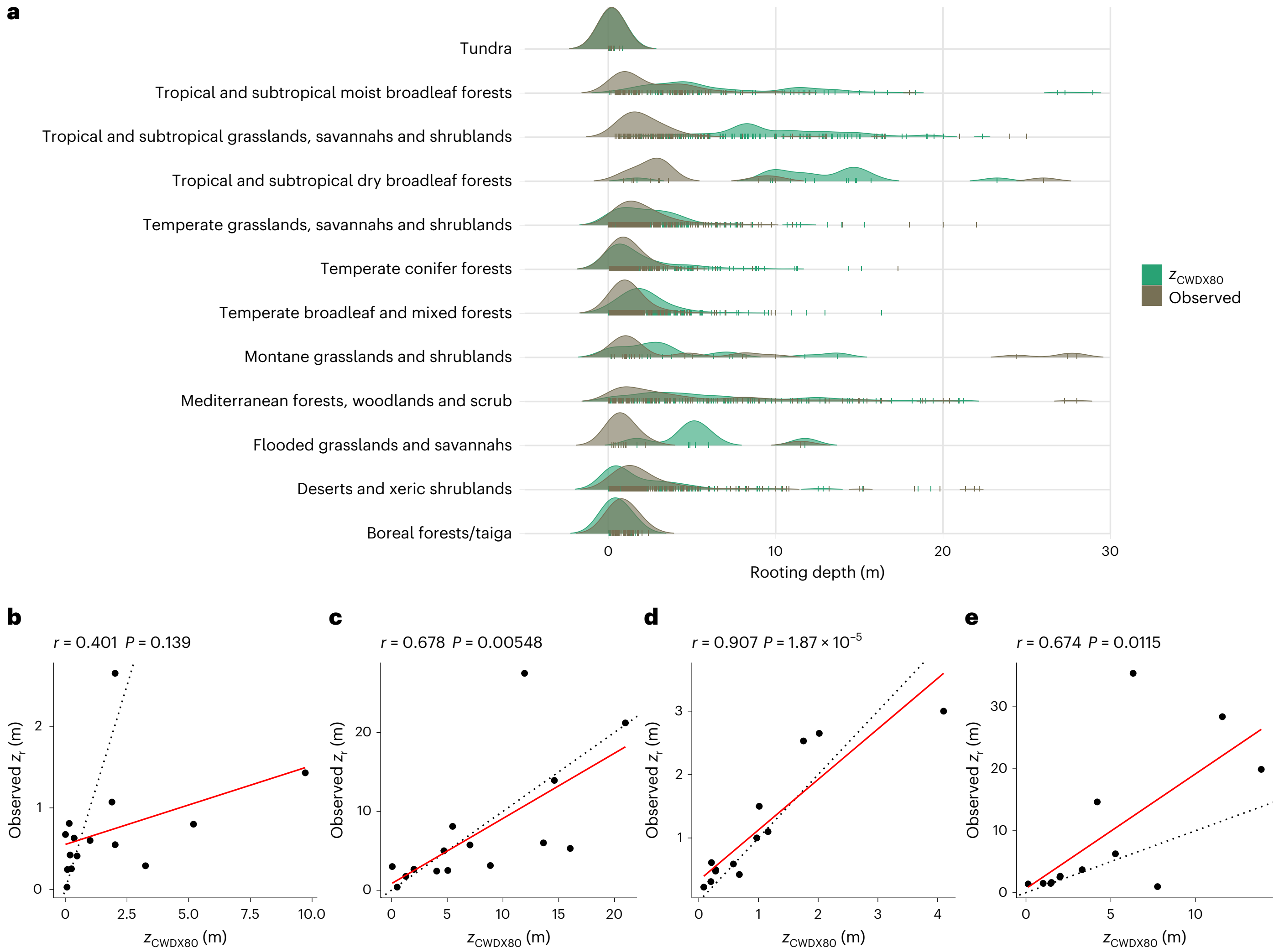

Fig. 4 | Modelled and observed rooting depth by biome. a, Kernel density estimates of observed and predicted (z_{CWDX80}) rooting depth by biome, based on data aggregated by sites, shown by vertical coloured tick marks. **b**–**e**, The 10% (**b**,**d**) and 90% (**c**,**e**) quantiles of observed versus predicted (z_{CWDX80}) rooting depth by biome of all data (**b**,**c**) and of a subset of the data where the WTD was measured along with rooting depth (**d**,**e**). Classification of sites into biomes was done on the basis of ref. [43]. Dotted lines in **b**–**e** represent the 1/1 line. *r* is the Pearson's correlation coefficient, and *P* is the test statistic based on Pearson's product moment correlation coefficient.

More fine-grained variations in S_0 within regions and biomes are linked to land use and irrigation of agricultural land (Fig. 2), to topography (Extended Data Figs. 7 and 8) and to the WTD, as indicated by the comparison with plant-level rooting-depth observations. The method applied here makes use of the sensitivity of remotely sensed ET to an increasing CWD and thus provides estimates of S_0 even if below-ground water stores are never fully depleted during the observational period. Additional analyses, where S_0 was diagnosed from a simple water-balance model with prescribed S_0, confirmed the reliability of the method across a broad range of hydroclimates (Supplementary Text 2 and Supplementary Fig. 5).

The S_0 reflects a combination of biotic and abiotic factors. Biotic factors that determine the total plant-available water are, for example, the rooting depth of the vegetation and plant hydraulic properties. Abiotic factors include the hydroclimate and physical constraints to the rooting depth, related to the texture and depth of the soil and the weathered bedrock[7]. Similarly, human management activities such as irrigation and tile drainage can impact ET, and thus S_0, in agricultural systems. Physical constraints to roots are largely unknown across large scales. Our estimation of S_0 makes no assumptions about such constraints. Instead, the magnitude of the water-storage capacity is inferred from mass-balance considerations. The CWD we derive from the balances of ET and *P* imply that the corresponding amount of water is supplied by local storage or supplied from lateral subsurface water convergence—likely a smaller contributor at the ~5 km spatial resolution of the data analysed here[35].

Diagnosed values of S_0 implicitly include water intercepted by leaf and branch surfaces, internal plant water storage and moisture stored in the topsoil and supplied to soil evaporation. These components are generally smaller in magnitude compared with moisture storage supplied to transpiration[36], and their contribution to ET declines rapidly as CWD increases. Hence, spatial variations in S_0 reflect primarily variations mediated by moisture stored across the root zone.

Particularly in regions with pronounced dry seasons, our estimates of S_0 greatly exceed typical values of the total soil WHC when considering the top 1 or 2 m of the soil column and texture information from global databases[31] (Extended Data Fig. 5). The discrepancy in magnitude and spatial patterns of total 1 (2) m soil WHC and S_0 diagnosed here hints at a critical role of plant access to deep water and the need to extend the focus beyond moisture in the top 1–2 m of soil for understanding and simulating land–atmosphere exchange[10,11]. Indications of widespread plant access to deep water stores are consistent with observations of bedrock-penetrating roots[7,37] and with evidence for dry-season moisture withdrawal from the weathered bedrock[9,11]. We note that using the global map of S_{CWDX80} (z_{CWDX80}) for directly parameterizing S_0 (z_{r}) in models may be misleading in areas with particularly small maximum CWDs and consequently small S_{CWDX80}. Scaling relationships of above- and below-ground plant architecture[30] and additional effects of how z_{r} determines access to below-ground resources and function (for example, nutrients and mechanical stability) should be considered.

Underlying the estimates of S_{CWDX80} is the assumption that plant rooting strategies are reflected by CWD extremes with a return period $T = 80$ yr; S_{dSIF} and S_{dEF} provide an independent constraint to test this assumption. Extended Data Fig. 4 suggests that T is not a global constant. A tendency towards higher T emerges with an increasing grid-cell average forest-cover fraction.

Our analysis identified mountain regions as being characterized by particularly high S_0, despite shallow soil and regolith depths[38]. This could be due to hillslope-scale variations in groundwater depth, enabling sustained transpiration during prolonged rain-free periods. Lateral subsurface flow at scales beyond the resolution of the data used here (~5 km) may additionally supply water for ET and thus contribute to large inferred S_0 in valley bottoms of large drainage basins. Local convergence (divergence) acts to supply (remove) subsurface moisture and sustain (reduce) ET, leading to larger (smaller) CWD values. Without relying on a priori assumptions regarding S_0 or functional dependencies of water stress effect on ET, thermal infrared- (TIR-) based remote-sensing data (as used here) offer an opportunity to detect such effects[8]. Our analysis yielded strong contrasts in diagnosed S_0 along topographic gradients (Extended Data Figs. 7 and 8). However, further research should assess the accuracy of spatial variations in annual mean ET and potential effects of terrain, where land surface temperature signals on shaded slopes may be misinterpreted by the ALEXI algorithm as signatures of higher ET.

Our global S_0 estimates are a ‘snapshot’ in time. Regional- to continental-scale variations in average tree ages may be associated with changes in rooting depth and S_0. Furthermore, environmental change may trigger changes in vegetation composition and structure[39], with consequences for S_0. Similarly, deforestation implies changes in rooting depth[18], S_0 and the surface energy balance[14]. Such temporal changes are not considered here due to the limited length of available time series of satellite observations (16 yr). It remains to be seen whether plasticity in z_{r} is sufficiently rapid to keep pace with a changing climate with strong and widespread increases in rainfall variability[40] and to what degree rising CO_2 alters plant water use and their carbon economy and thereby the costs and benefits of deep roots.

Taken together, constraints available from local z_{r} observations and from global remote sensing of vegetation activity reveal consistent patterns across multiple spatial scales and suggest widespread plant access to deep water storage, including the weathered bedrock and groundwater, or to other ancillary sources of water, such as irrigation. Our study revealed a tight link of the climatology of water deficits and vegetation sensitivity to drought stress. We demonstrated how land–atmosphere interactions and the critical zone water-storage capacity are linked with the rooting depth of vegetation and how below-ground vegetation structure is influenced by the hydroclimate and topography across the globe.

Online content

Any methods, additional references, Nature Portfolio reporting summaries, source data, extended data, supplementary information, acknowledgements, peer review information; details of author contributions and competing interests; and statements of data and code availability are available at https://doi.org/10.1038/s41561-023-01125-2.

References

1. Teuling, A. J., Seneviratne, S. I., Williams, C. & Troch, P. A. Observed timescales of evapotranspiration response to soil moisture. *Geophys. Res. Lett.* **33**, L23403 (2006).
2. Gao, H. et al. Climate controls how ecosystems size the root zone storage capacity at catchment scale. *Geophys. Res. Lett.* **41**, 7916–7923 (2014).
3. Milly, P. C. D. Climate, soil water storage, and the average annual water balance. *Water Resour. Res.* **30**, 2143–2156 (1994).
4. Hahm, W. J. et al. Low subsurface water storage capacity relative to annual rainfall decouples Mediterranean plant productivity and water use from rainfall variability. *Geophys. Res. Lett.* **46**, 6544–6553 (2019).
5. Seneviratne, S. I. et al. Investigating soil moisture–climate interactions in a changing climate: a review. *Earth Sci. Rev.* **99**, 125–161 (2010).
6. Thompson, S. E. et al. Comparative hydrology across AmeriFlux sites: the variable roles of climate, vegetation, and groundwater. *Water Resour. Res.* **47**, W00J07 (2011).
7. Fan, Y., Miguez-Macho, G., Jobbágy, E. G., Jackson, R. B. & Otero-Casal, C. Hydrologic regulation of plant rooting depth. *Proc. Natl Acad. Sci. USA* **114**, 10572–10577 (2017).
8. Hain, C. R., Crow, W. T., Anderson, M. C. & Tugrul Yilmaz, M. Diagnosing neglected soil moisture source–sink processes via a thermal infrared-based two-source energy balance model. *J. Hydrometeorol.* **16**, 1070–1086 (2015).
9. Rempe, D. M. & Dietrich, W. E. Direct observations of rock moisture, a hidden component of the hydrologic cycle. *Proc. Natl Acad. Sci. USA* **115**, 2664–2669 (2018).
10. Dawson, T. E., Jesse Hahm, W. & Crutchfield-Peters, K. Digging deeper: what the critical zone perspective adds to the study of plant ecophysiology. *N. Phytol.* **226**, 666–671 (2020).
11. McCormick, E. L. et al. Widespread woody plant use of water stored in bedrock. *Nature* **597**, 225–229 (2021).
12. Maxwell, R. M. & Condon, L. E. Connections between groundwater flow and transpiration partitioning. *Science* **353**, 377–380 (2016).
13. Schlemmer, L., Schär, C., Lüthi, D. & Strebel, L. A groundwater and runoff formulation for weather and climate models. *J. Adv. Model. Earth Syst.* **10**, 1809–1832 (2018).
14. Teuling, A. J. et al. Contrasting response of European forest and grassland energy exchange to heatwaves. *Nat. Geosci.* **3**, 722–727 (2010).
15. Koirala, S. et al. Global distribution of groundwater–vegetation spatial covariation. *Geophys. Res. Lett.* **44**, 4134–4142 (2017).
16. Esteban, E. J. L., Castilho, C. V., Melgaço, K. L. & Costa, F. R. C. The other side of droughts: wet extremes and topography as buffers of negative drought effects in an Amazonian forest. *N. Phytol.* **229**, 1995–2006 (2021).
17. Liu, Y., Konings, A. G., Kennedy, D. & Gentine, P. Global coordination in plant physiological and rooting strategies in response to water stress. *Glob. Biogeochem. Cycles* **35**, e2020GB006758 (2021).
18. Schenk, H. J. & Jackson, R. B. The global biogeography of roots. *Ecol. Monogr.* **72**, 311–328 (2002).
19. Canadell, J. et al. Maximum rooting depth of vegetation types at the global scale. *Oecologia* **108**, 583–595 (1996).
20. Weaver, J. E. & Darland, R. W. Soil–root relationships of certain native grasses in various soil types. *Ecol. Monogr.* **19**, 303–338 (1949).
21. Chitra-Tarak, R. et al. Hydraulically-vulnerable trees survive on deep-water access during droughts in a tropical forest. *N. Phytol.* **231**, 1798–1813 (2021).
22. Schenk, H. J. & Jackson, R. B. Mapping the global distribution of deep roots in relation to climate and soil characteristics. *Geoderma* **126**, 129–140 (2005).

23. Franklin, O. et al. Organizing principles for vegetation dynamics. *Nat. Plants* **6**, 444–453 (2020).
24. Kleidon, A. & Heimann, M. A method of determining rooting depth from a terrestrial biosphere model and its impacts on the global water and carbon cycle. *Glob. Change Biol.* **4**, 275–286 (1998).
25. Schymanski, S. J., Sivapalan, M., Roderick, M. L., Hutley, L. B. & Beringer, J. An optimality-based model of the dynamic feedbacks between natural vegetation and the water balance. *Water Resour. Res.* **45**, W01412 (2009).
26. Wang-Erlandsson, L. et al. Global root zone storage capacity from satellite-based evaporation. *Hydrol. Earth Syst. Sci.* **20**, 1459–1481 (2016).
27. Knapp, A. K. & Smith, M. D. Variation among biomes in temporal dynamics of aboveground primary production. *Science* **291**, 481–484 (2001).
28. Anderson, M. A two-source time-integrated model for estimating surface fluxes using thermal infrared remote sensing. *Remote Sens. Environ.* **60**, 195–216 (1997).
29. Hain, C. R. & Anderson, M. C. Estimating morning change in land surface temperature from MODIS day/night observations: applications for surface energy balance modeling. *Geophys. Res. Lett.* **44**, 9723–9733 (2017).
30. Tumber-Dávila, S. J., Schenk, H. J., Du, E. & Jackson, R. B. Plant sizes and shapes above- and belowground and their interactions with climate. *New Phytol*. https://nph.onlinelibrary.wiley.com/doi/abs/10.1111/nph.18031 (2022).
31. *Harmonized World Soil Database* Version 1.0 (FAO, 2008).
32. Wieder, W. *Regridded Harmonized World Soil Database* Version 1.2 (ORNL DAAC, 2014); https://doi.org/10.3334/ORNLDAAC/1247
33. Balland, V., Pollacco, J. A. P. & Arp, P. A. Modeling soil hydraulic properties for a wide range of soil conditions. *Ecol. Model.* **219**, 300–316 (2008).
34. Agee, E. et al. Root lateral interactions drive water uptake patterns under water limitation. *Adv. Water Resour.* **151**, 103896 (2021).
35. Krakauer, N. Y., Li, H. & Fan, Y. Groundwater flow across spatial scales: importance for climate modeling. *Environ. Res. Lett.* **9**, 034003 (2014).
36. Stoy, P. C. et al. Reviews and syntheses: turning the challenges of partitioning ecosystem evaporation and transpiration into opportunities. *Biogeosciences* **16**, 3747–3775 (2019).
37. Jackson, R. B., Moore, L. A., Hoffmann, W. A., Pockman, W. T. & Linder, C. R. Ecosystem rooting depth determined with caves and DNA. *Proc. Natl Acad. Sci. USA* **96**, 11387–11392 (1999).
38. Pelletier, J. D. et al. A gridded global data set of soil, intact regolith, and sedimentary deposit thicknesses for regional and global land surface modeling. *J. Adv. Model. Earth Syst.* **8**, 41–65 (2016).
39. Parmesan, C. & Hanley, M. E. Plants and climate change: complexities and surprises. *Ann. Bot.* **116**, 849–864 (2015).
40. Pendergrass, A. G., Knutti, R., Lehner, F., Deser, C. & Sanderson, B. M. Precipitation variability increases in a warmer climate. *Sci. Rep.* **7**, 17966 (2017).
41. Siebert, S. et al. Development and validation of the global map of irrigation areas. *Hydrol. Earth Syst. Sci.* **9**, 535–547 (2005).
42. Friedl, M. A. et al. MODIS Collection 5 global land cover: Algorithm refinements and characterization of new datasets. *Remote Sens. Environ.* **114**, 168–182 (2010).
43. Olson, D. M. et al. Terrestrial ecoregions of the world: a new map of life on Earth. *BioScience* **51**, 933–938 (2001).

Methods

Estimating ET

Unbiased estimates of ET during rain-free periods are essential for determining CWD and estimating S_0 and implied z_r. We tested different remote-sensing-based ET products and found that the ALEXI-TIR product, which is based on TIR remote sensing[28,29], exhibits no systematic bias during progressing droughts (Supplementary Text 3 and Supplementary Fig. 6), in contrast to other ET estimates assessed here. The stability in ET estimates from ALEXI-TIR during drought is enabled by its effective use of information about the surface energy partitioning, allowing inference of ET rates without reliance on a priori specified and inherently uncertain surface conductances[44] or shapes of empirical water stress functions[45], and without assumptions of rooting depth or effective S_0. ALEXI-TIR is thus well suited for estimating actual ET behaviour during drought without introducing circularity in inferring S_0.

CWD estimation

The CWD is determined here from the cumulative difference of actual ET and the liquid-water infiltration to the soil (P_{in}). ET is based on thermal infrared remote sensing, provided by the global ALEXI data product at daily and 0.05° resolution, covering years 2003–2018. Values in energy units of the latent heat flux are converted to mass units accounting for the temperature and air-pressure dependence of the latent heat of vaporization following ref. [46]. The P_{in} is based on daily reanalysis data of P in the form of rain and snow from WATCH-WFDEI[47]. A simple snow accumulation and melt model[48] is applied to account for the effect of snowpack as a temporary water storage that supplies P_{in} during spring and early summer. Snow melt is assumed to occur above 1 °C and with a rate of 1 mm d^{-1} °C^{-1}. The CWD is derived by applying a running sum of (ET − P_{in}), initiating on the first day when (ET − P_{in}) is positive (net water loss from the soil) and terminating the summation after rain has reduced the running sum to zero (Supplementary Fig. 7). This yields a continuous CWD time series of daily values. In general, $P >$ ET for annual totals. This implies that the CWD summation is initiated at zero each year. In very rare cases, the CWD accumulates over more than one year, and data were discarded if the accumulation extended over five years ('runaway CWD'). All P and snow melt (P_{in}) are assumed to contribute to reducing the CWD. This implicitly assumes that no run-off occurs while the CWD is above zero. The period between the start and end of accumulation is referred to as a CWD event. Within each event, co-varying data, used for analysis, are removed after rain has reduced the CWD to below 90% of its maximum value within the same event. This concerns the analysis of SIF and EF (see the following) and avoids effects of relieved water stress by re-wetting topsoil layers before the CWD is fully compensated. The algorithm to determine daily CWD values and events is implemented by the R package *cwd*[49].

Diagnosing S_0 from vegetation activity

By employing first principles for the constraint of the rooting-zone water availability on vegetation activity[1], we developed a method to derive how the sensitivity of these fluxes to water stress relates to S_0 and how this sensitivity can be used to reveal effects of access to extensive deep water stores. Two methodologically independent sources of information on vegetation activity were used: EF (defined as ET divided by net radiation) and SIF (normalized by incident short-wave radiation). SIF is a proxy for ecosystem photosynthesis[50] and is taken here from a spatially downscaled data product[51] based on GOME-2 data[52,53]. Since net radiation and short-wave radiation are first-order controls on ET and SIF, respectively, and to avoid effects by seasonally varying radiation inputs, we used EF instead of ET and considered the ecosystem-level fluorescence yield, quantified as SIF divided by short-wave radiation (henceforth referred to as 'SIF') for all analyses. The resulting estimates for S_0 are referred to as S_{dEF} and S_{dSIF}, respectively.

The principles for relating vegetation activity to the rooting-zone water availability were considered as follows. As the ecosystem-level CWD increases, both gross primary production (ecosystem-level photosynthesis) and ET are limited by the availability of water to plants. In the following, we refer to gross primary production and ET as a generic 'vegetation activity' variable $X(t)$. This principle can be formulated, in its simplest form, as a model of $X(t)$ being a linear function of the remaining water stored along the rooting zone $S(t)$, expressed as a fraction of the total rooting-zone water-storage capacity S_0:

$$X(t) = X_0 \times S(t)/S_0 \tag{1}$$

Following equation (1), S_0 can be interpreted as the total rooting-zone water-storage capacity, or the depth of a water bucket that supplies moisture for ET. Following ref. [1] and with $X(t)$ representing ET, the temporal dynamics during rain-free periods (where run-off can be neglected) are described by the differential equation

$$\mathrm{d}S/\mathrm{d}t = -X(t) \Rightarrow \mathrm{d}S/\mathrm{d}t = -X_0 \times S(t)/S_0 \tag{2}$$

and solved by an exponential function with a characteristic decay timescale λ:

$$X(t) = X_0 \times \exp(-[t - t_0]/\lambda) \tag{3}$$

λ is related to S_0 as $S_0 = \lambda X_0$, where X_0 is the initial ET at $S(t_0) = S_0$. In other words, the apparent observed exponential ET decay timescale λ, together with X_0, reflects the total rooting-zone water-storage capacity S_0.

Fitting exponentials from observational data is subject to assumptions regarding stomatal responses to declines in $S(t)$ and is relatively sensitive to data scatter. Hence, resulting estimates of S_0 may not be robust. With CWD(t) = $S_0 - S(t)$ and equation (1), the relationship of $X(t)$ and CWD(t) can be expressed as a linear function

$$X(t) = X_0 - X_0/S_0 \times \mathrm{CWD}(t) \tag{4}$$

and observational data for $X(t)$ can be used to fit a linear regression model. Its intercept a and slope b can then be used as an alternative, and potentially more robust, estimate for S_0:

$$S_0 = -a/b \tag{5}$$

This has the further advantage that estimates for S_0 can be derived using any observable quantity of vegetation activity $X(t)$ (not just ET as in ref. [1]) under the assumption that activity attains zero at the point when the CWD reaches the total rooting-zone water-storage capacity; that is, $X(t^*) = 0$ for CWD(t^*) = S_0.

Here we use a spatially downscaled product of SIF[51], normalized by incident short-wave radiation (WATCH-WFDEI data[47]), and the EF, defined as the ratio of ET (ALEXI-ET data[29]) over net radiation (GLASS data[54]), as two alternative, normalized proxies for water-constrained vegetation activity, termed X'. Normalization by net radiation and incident short-wave radiation, respectively, removes effects by seasonally varying energy available for vegetation activity. X'_0 is thus assumed to be stationary over time, and the relationship of $X'(t)$ and CWD(t) is interpreted here as a reflection of effects by below-ground water availability and used to derive S_{dSIF} and S_{dEF}. All data used for X'_0 are provided at 0.05° and daily resolution.

S_{dSIF} and S_{dEF} were then derived on the basis of the relationship of EF and normalized SIF versus CWD, guided by equation (5). The relationship was analysed for each pixel with pooled data belonging to the single largest CWD event of each year and using the 90% quantile of EF and normalized SIF within 50 evenly spaced bins along the CWD axis. Binning and considering percentiles were chosen to reduce effects of vegetation activity reduction due to factors other than water stress (CWD). We then tested, for each pixel, whether the data support the model of a single linear decline of SIF (EF) with increasing CWD (equation (5)) or, alternatively, a segmented regression model with one or two change points, using the R package *segmented*[55]. The model with the lowest Bayesian information criterion was chosen, and S_{dSIF} and S_{dEF} were quantified only for pixels where no significant change point was detected and where the regression of EF (SIF) versus CWD had a significantly negative slope. Flattening EF (SIF) versus CWD relationships were identified where a significant change point was detected and where the slope of the second regression segment was significantly less negative ($P = 0.05$ of t test) compared with the slope of the first segment. Examples, visualizing the diagnosing of S_0 from EF, are given in Supplementary Fig. 8. We performed additional tests of the method's reliability in estimating S_0 by deriving S_{dEF} from simulations of the ecosystem water balance and ET, where S_0 was prescribed, using the SPLASH (Simple Process-Led Algorithms for Simulating Habitats) model[46]. This demonstrates that the method applied for S_{dSIF} and S_{dEF} yields accurate estimates of S_0 across all climatic conditions and independent of the size of S_0 (Supplementary Text 2 and Supplementary Fig. 5).

Diagnosing S_0 from CWDs

Following ref.[2], the S_0 is estimated on the basis of CWD extremes occurring with a return period of T years. Magnitudes of extremes with a given return period T ($S_{\mathrm{CWDX}T}$) are estimated by fitting an extreme value distribution (Gumbel) to the annual maximum CWD values for each pixel separately, using the *extRemes* R package[56]. Values $S_{\mathrm{CWDX}T}$ are translated into an effective depth $z_{\mathrm{CWDX}T}$ using estimates of the plant-available soil WHC, on the basis of soil-texture data from a gridded version of the Harmonized World Soil Database[31,32] and pedo-transfer functions derived by ref.[33]. Associations of $S_{\mathrm{CWDX}T}$ and topography were analysed considering the Compound Topography Index[57] and elevation from ETOPO1[58]. The Compound Topography Index is a measure for subsurface flow convergence and the WTB based on the topographical setting[59].

Estimating return periods

Diagnosed values of S_{dSIF} and S_{dEF} provide a constraint on the return period T. To yield stable estimates of T and avoid effects of the strong nonlinearity of the function to derive T from the fitted extreme value distributions and magnitudes estimated by S_{dSIF} and S_{dEF}, we pooled estimates S_{dSIF} (S_{dEF}) and $S_{\mathrm{CWDX}T}$ values within 1° pixels (≤400 values). A range of discrete values T was screened (10, 20, 30, 40, 50, 60, 70, 80, 90, 100, 150, 200, 250, 300, 350, 400, 450, 500 yr), and the best estimate T was chosen on the basis of comparison with S_{dSIF} (T_{SIF}) and to S_{dEF} (T_{EF}), that is, where the absolute value of the median of the logarithm of the bias was minimal. Relationships of best matching T with topography (measured by the Compound Topography Index[57]) and with the forest-cover fraction (MODIS MOD44B[60]) were analysed.

Rooting-depth estimation and observations

We converted root-zone water-storage capacity estimates, S_{CWDX80}, to a corresponding apparent rooting depth (z_{CWDX80}) using a global soil-texture map[31,32]. The conversion of S_{CWDX80} into a corresponding depth z_{CWDX80} accounts for topsoil and subsoil texture and WHC along the rooting profile (Methods and Fig. 3b) and, in view of lacking information with global coverage about the WHC of the weathered bedrock, assuming uniform subsoil texture extending below 30 cm depth. The comparison of biome-level quantities (instead of a direct point-by-point comparison) avoids the inevitable scale mismatch between in situ plant-level observations and global remote-sensing data.

The observational rooting-depth dataset ($N = 5{,}524$) was compiled by ref.[30] by combining and complementing published datasets from refs.[22,7]. The data include observations of the maximum rooting depth of plants taken from 361 published studies plus additional environmental and climate data. The z_{r} was taken as the plant's maximum rooting depth. Data were aggregated by sites ($N = 1{,}705$) on the basis of longitude and latitude information. Sites were classified into biomes using maps of terrestrial ecoregions[43]. Quantiles (10%, 90%) were determined for each biome. For a subset of the data (359 sites) where parallel measurements of the WTD were available, we conducted the same analysis but took the minimum of WTD and z_{r}.

Data availability

Global datasets of S_{CWDX80} and z_{CWDX80} are available on *Zenodo*[61]. The rooting-depth data are published separately[30].

Code availability

The CWD calculation from ET and P_{in} time series is implemented by the R package *cwd*[49]. All code for this analysis is published on *Zenodo*[62].

References

44. Mu, Q., Heinsch, F. A., Zhao, M. & Running, S. W. Development of a global evapotranspiration algorithm based on MODIS and global meteorology data. *Remote Sens. Environ.* **111**, 519–536 (2007).
45. Fisher, J. B. et al. ECOSTRESS: NASA's next generation mission to measure evapotranspiration from the international space station. *Water Resour. Res.* **56**, e2019WR026058 (2020).
46. Davis, T. W. et al. Simple process-led algorithms for simulating habitats (SPLASH v.1.0): robust indices of radiation, evapotranspiration and plant-available moisture. *Geosci. Model Dev.* **10**, 689–708 (2017).
47. Weedon, G. P. et al. The WFDEI meteorological forcing data set: WATCH forcing data methodology applied to ERA-Interim reanalysis data. *Water Resour. Res.* **50**, 7505–7514 (2014).
48. Orth, R., Koster, R. D. & Seneviratne, S. I. Inferring soil moisture memory from streamflow observations using a simple water balance model. *J. Hydrometeorol.* **14**, 1773–1790 (2013).
49. Stocker, B. cwd v.1.0: R package for cumulative water deficit calculation. *Zenodo* https://doi.org/10.5281/zenodo.5359053 (2021).
50. Zhang, Y. et al. Model-based analysis of the relationship between sun-induced chlorophyll fluorescence and gross primary production for remote sensing applications. *Remote Sens. Environ.* **187**, 145–155 (2016).
51. Duveiller, G. et al. A spatially downscaled sun-induced fluorescence global product for enhanced monitoring of vegetation productivity. *Earth Syst. Sci. Data* **12**, 1101–1116 (2020).
52. Joiner, J. et al. Global monitoring of terrestrial chlorophyll fluorescence from moderate-spectral-resolution near-infrared satellite measurements: methodology, simulations, and application to GOME-2. *Atmos. Meas. Tech.* **6**, 2803–2823 (2013).
53. Köhler, P., Guanter, L. & Joiner, J. A linear method for the retrieval of sun-induced chlorophyll fluorescence from GOME-2 and SCIAMACHY data. *Atmos. Meas. Tech.* **8**, 2589–2608 (2015).
54. Jiang, B. et al. Validation of the surface daytime net radiation product from version 4.0 GLASS product suite. *IEEE Geosci. Remote Sens. Lett.* **16**, 509–513 (2019).
55. Muggeo, V. M. R. Estimating regression models with unknown break-points. *Stat. Med.* **22**, 3055–3071 (2003).
56. Gilleland, E. & Katz, R. W. extRemes 2.0: an extreme value analysis package in R. *J. Stat. Softw.* **72**, 1–39 (2016).
57. Marthews, T. R., Dadson, S. J., Lehner, B., Abele, S. & Gedney, N. High-resolution global topographic index values for use in large-scale hydrological modelling. *Hydrol. Earth Syst. Sci.* **19**, 91–104 (2015).
58. *Etopo1, Global 1 Arc-Minute Ocean Depth and Land Elevation from the US National Geophysical Data Center (NGDC)* (National Geophysical Data Center, NESDIS, NOAA and US Department of Commerce, 2011); https://doi.org/10.5065/D69Z92Z5

59. Beven, K. J. & Kirkby, M. J. A physically based, variable contributing area model of basin hydrology. *Hydrol. Sci. J.* **24**, 43–69 (1979).
60. Hansen, M. C., Townshend, J. R. G., DeFries, R. S. & Carroll, M. Estimation of tree cover using MODIS data at global, continental and regional/local scales. *Int. J. Remote Sens.* **26**, 4359–4380 (2005).
61. Stocker, B. D. Global rooting zone water storage capacity and rooting depth estimates. *Zenodo* https://doi.org/10.5281/zenodo.5515246 (2021).
62. Stocker, B. stineb/mct: v3.0: re-submission to *Nature Geoscience*. *Zenodo* https://doi.org/10.5281/zenodo.6239187 (2022).

Acknowledgements

B.D.S. was funded by the Swiss National Science Foundation grant no. PCEFP2_181115. This work is a contribution to the LEMONTREE (Land Ecosystem Models Based On New Theory, Observations and Experiments) project, funded through the generosity of Eric and Wendy Schmidt by recommendation of the Schmidt Futures programme (B.D.S.). We acknowledge ICDC, CEN, University of Hamburg for data support. S.J.T.-D. was funded by the NSF GRFP and LTER and the NASEM Ford Foundation Fellowship Program. A.G.K. was supported by NSF DEB-1942133.

Author contributions

B.D.S. developed the methods, conducted the analysis and wrote the paper. S.J.T.-D. compiled the rooting-depth dataset and guided its analysis. A.G.K. helped design the analysis and paper. M.C.A. developed the algorithm for thermal infrared remote sensing of evapotranspiration. C.H. generated the evapotranspiration dataset. R.B.J. initiated the study and guided the analysis. All authors contributed to writing the paper.

Funding

Open access funding provided by University of Bern.

Competing interests

The authors declare no competing interests.

Additional information

Extended data is available for this paper at https://doi.org/10.1038/s41561-023-01125-2.

Supplementary information The online version contains supplementary material available at https://doi.org/10.1038/s41561-023-01125-2.

Correspondence and requests for materials should be addressed to Benjamin D. Stocker.

Peer review information *Nature Geoscience* thanks Daniella Rempe, David Dralle and the other, anonymous, reviewer(s) for their contribution to the peer review of this work. Primary Handling Editor: Tamara Goldin, in collaboration with the *Nature Geoscience* team.

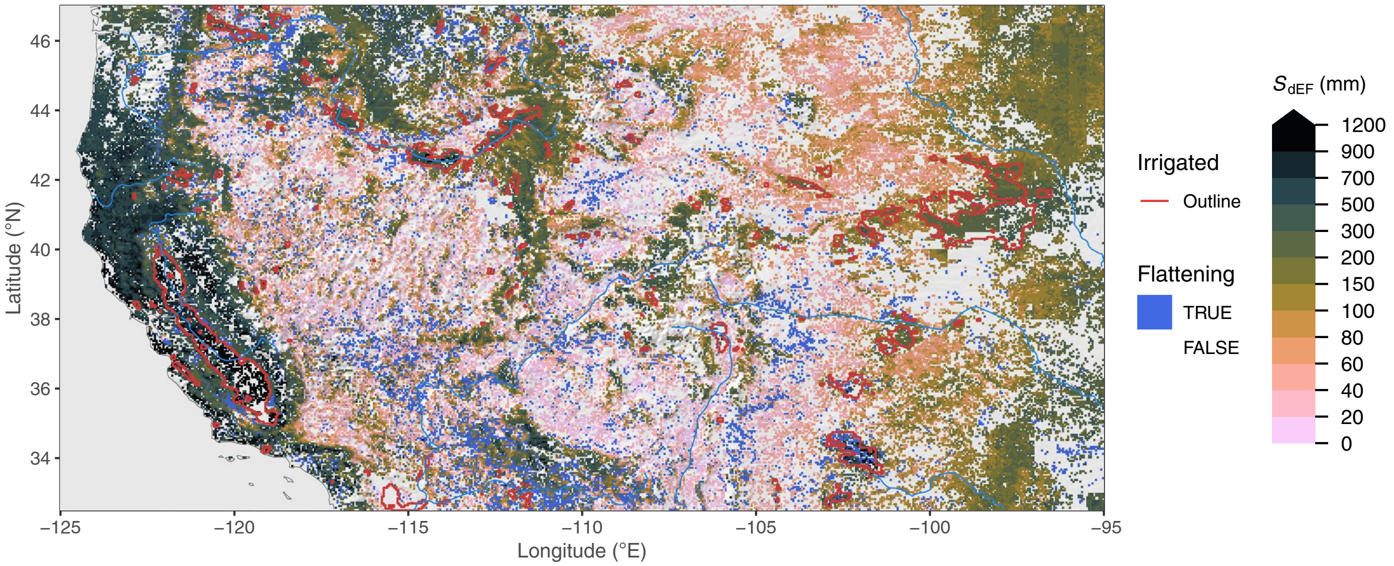

Extended Data Fig. 1 | Rooting zone water storage capacity in the Western USA. Estimated from the evaporative fraction (S_{dEF}). Blue areas ('flattening') show grid cells where a significant reduction in the slope in EF vs. CWD was identified beyond a certain threshold. Red lines show outlines of major irrigated areas, that is, where the irrigated land area fraction is above 30%[39]. Blank grid cells indicate areas with a sustained imbalance of ET being greater than *P*.

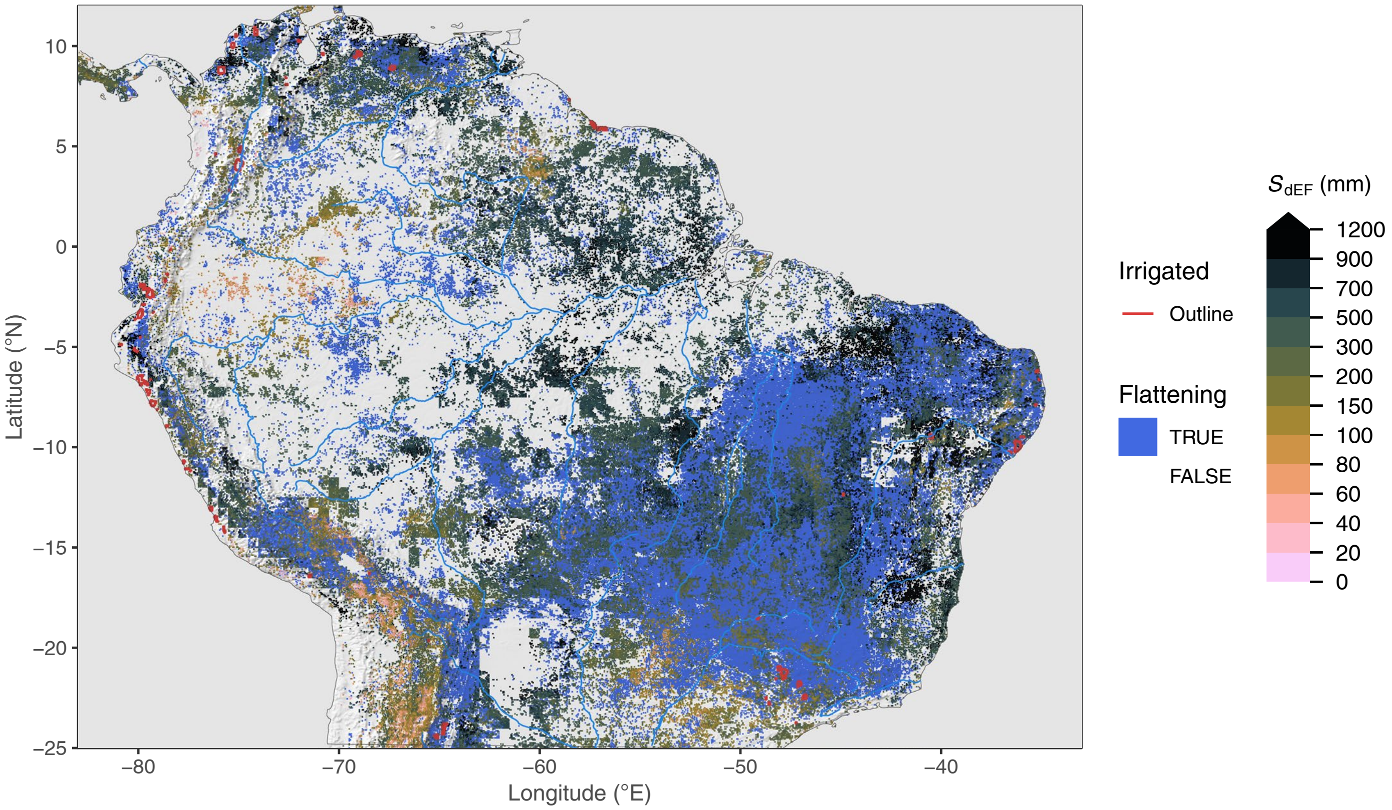

Extended Data Fig. 2 | Rooting zone water storage capacity in the Amazon region. Estimated from the evaporative fraction (S_{dEF}). Blue areas ('flattening') show grid cells where a significant reduction in the slope in EF vs. CWD was identified beyond a certain threshold. Red lines show outlines of major irrigated areas, that is, where the irrigated land area fraction is above 30%[39]. Blank grid cells indicate areas with a sustained imbalance of ET being greater than *P*.

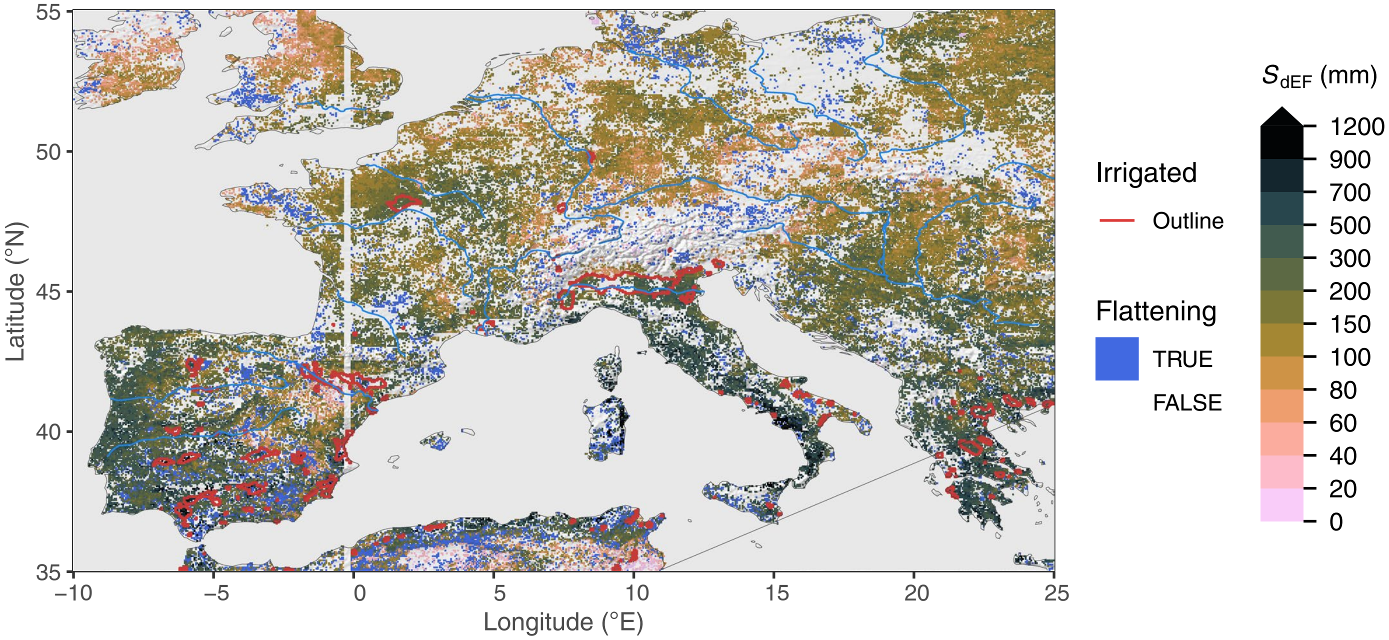

Extended Data Fig. 3 | Rooting zone water storage capacity in Europe. Estimated from the evaporative fraction (S_{dEF}). Blue areas ('flattening') show grid cells where a significant reduction in the slope in EF vs. CWD was identified beyond a certain threshold. Red lines show outlines of major irrigated areas, that is, where the irrigated land area fraction is above 30%[39]. Blank grid cells indicate areas with a sustained imbalance of ET being greater than *P*.

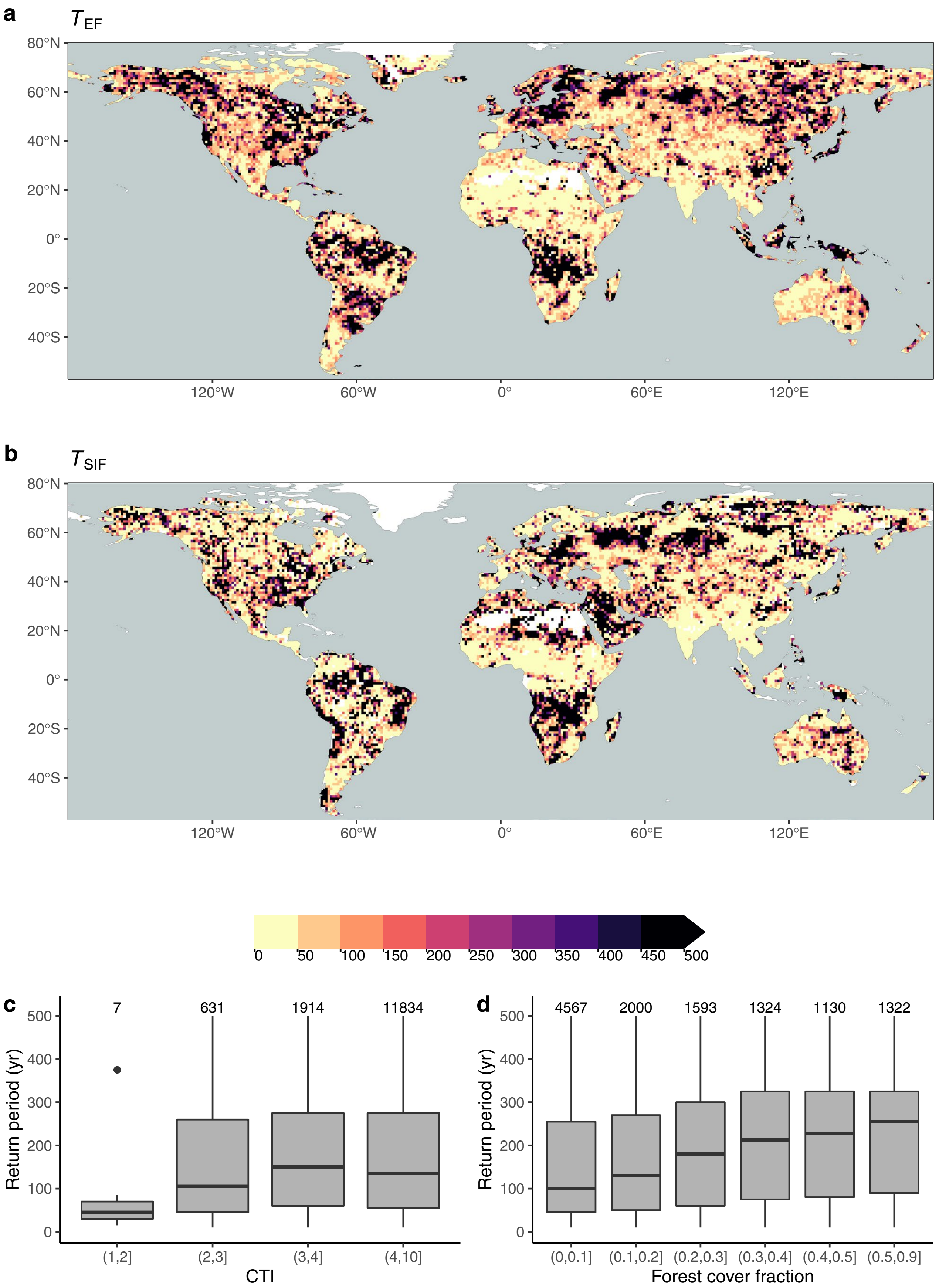

Extended Data Fig. 4 | See next page for caption.

Extended Data Fig. 4 | Return periods diagnosed from the evaporative fraction and sun-induced fluorescence. Return periods T (yr), diagnosed from EF (a) and SIF (b). To diagnose T, a range of alternative values of T are screened and the corresponding range of values $S_{\mathrm{CWDX}T}$ are compared to S_{dEF} S_{dSIF}) within 1° grid cells (resolution of maps shown here). The best matching T was retained for each gridcell, yielding a global distribution of T_{EF} (T_{SIF}). The bottom panel shows the distribution of diagnosed return periods T (mean of T_{EF} and T_{SIF}) within bins of the Compound Topography Index[60] (c) and forest cover fractions (MOD44B[62]) (d). Boxes represent the interquartile ranges of binned values (Q_{25}, Q_{75}), and whiskers cover $Q_{25} - 1.5(Q_{75} - Q_{25})$ to $Q_{75} + 1.5(Q_{75} - Q_{25})$. Numbers of data points per bin are given above boxes.

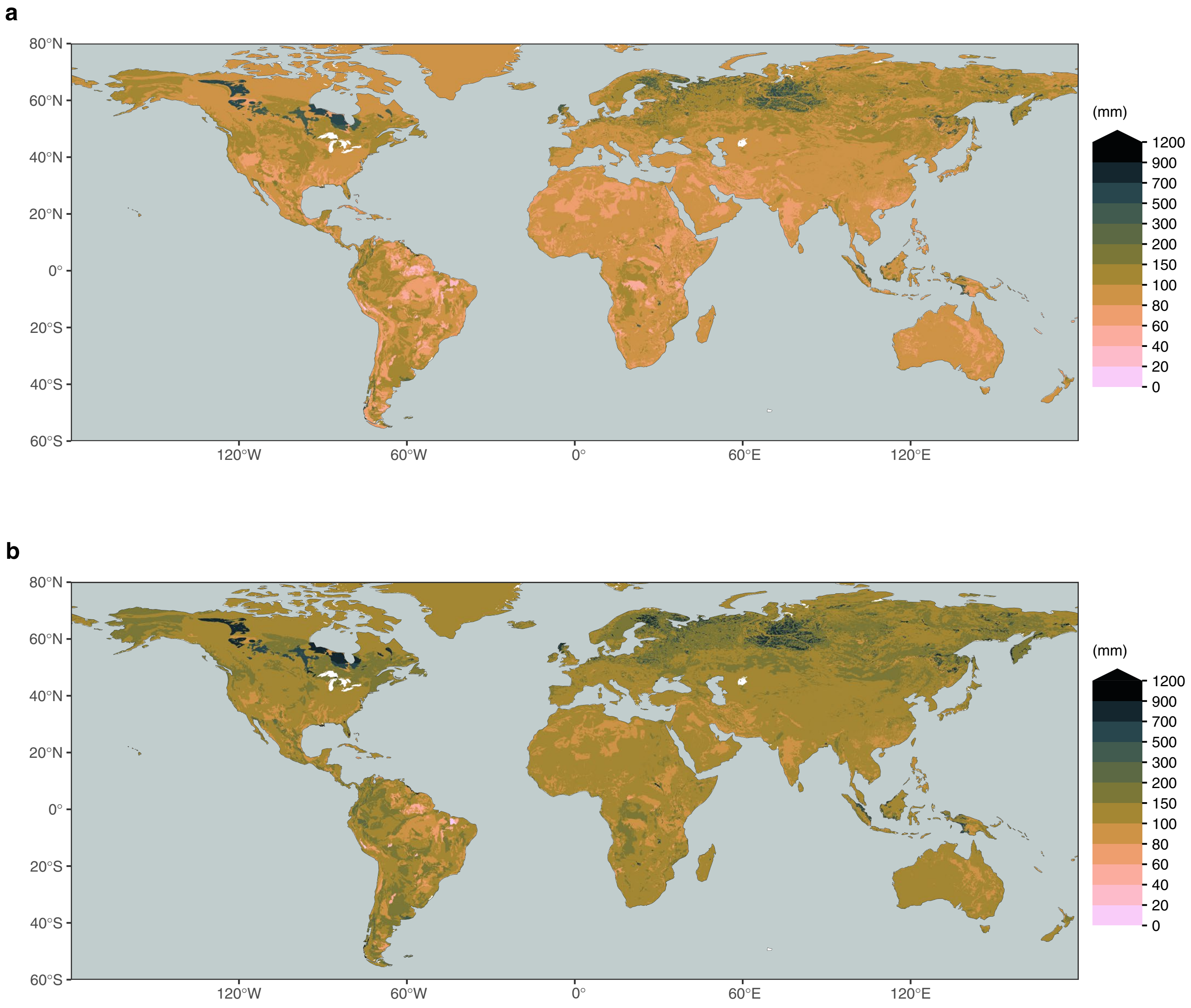

Extended Data Fig. 5 | Integrated soil water holding capacity in the soil. Integrated soil water holding capacity across the top 1 m (a) and the top 2 m (b). Values are calculated based on soil texture information from a gridded version[30] of the Harmonized World Soil Database[29] and pedo-transfer functions based on ref. [31]. HWSD provides information for a top layer (0-30 cm depth) and a bottom layer (30-100 cm depth). For the top 2 m shown in (b), we assumed values from the bottom layer for 100-200 cm depth.

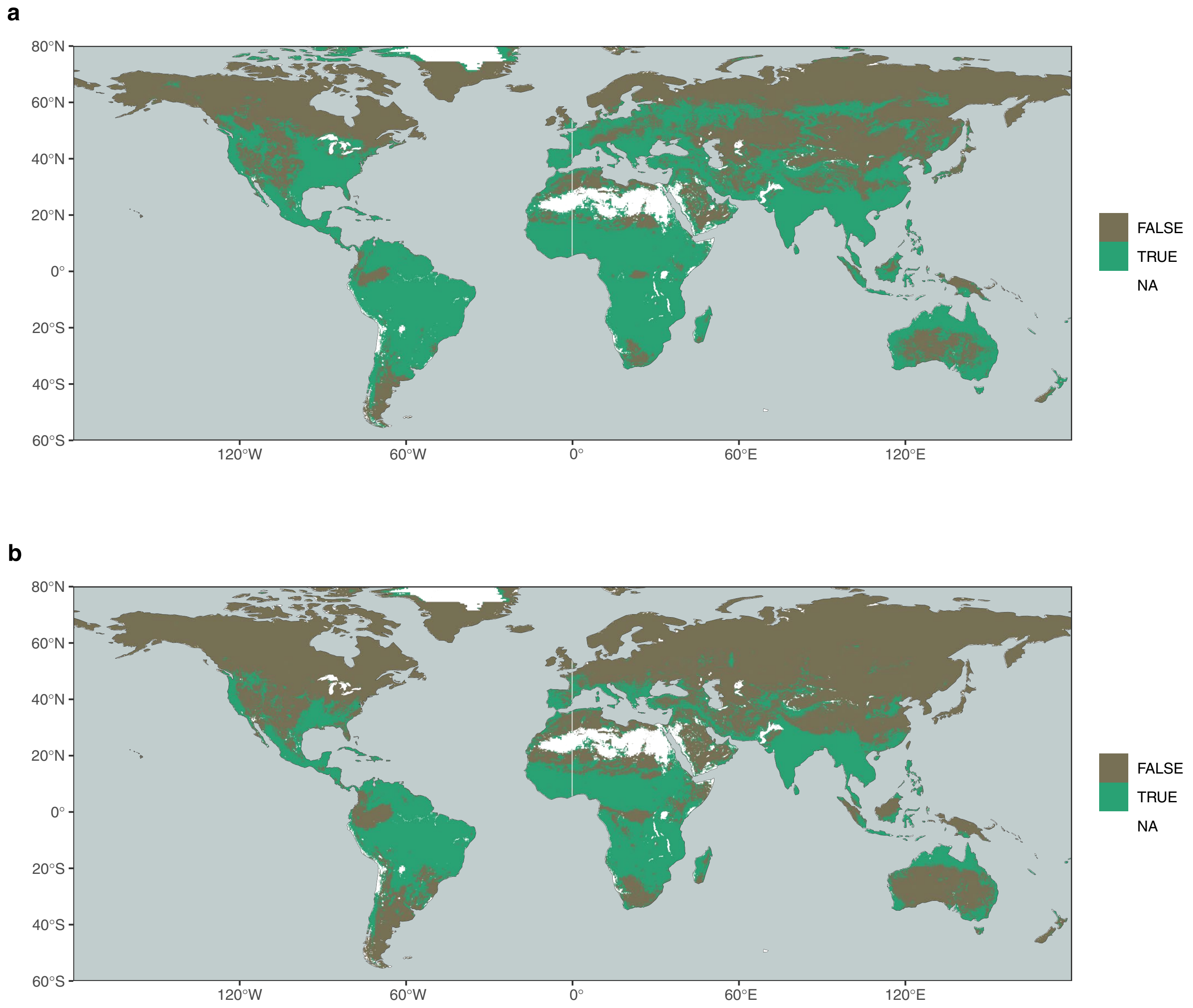

Extended Data Fig. 6 | Locations of plant access to deep water storage. Plant access to deep water storage. Green colors indicate regions where S_{CWDX80} suggests a rooting zone water storage capacity larger than the integrated water holding capacity across the top 1 m (a) and 2 m (b).

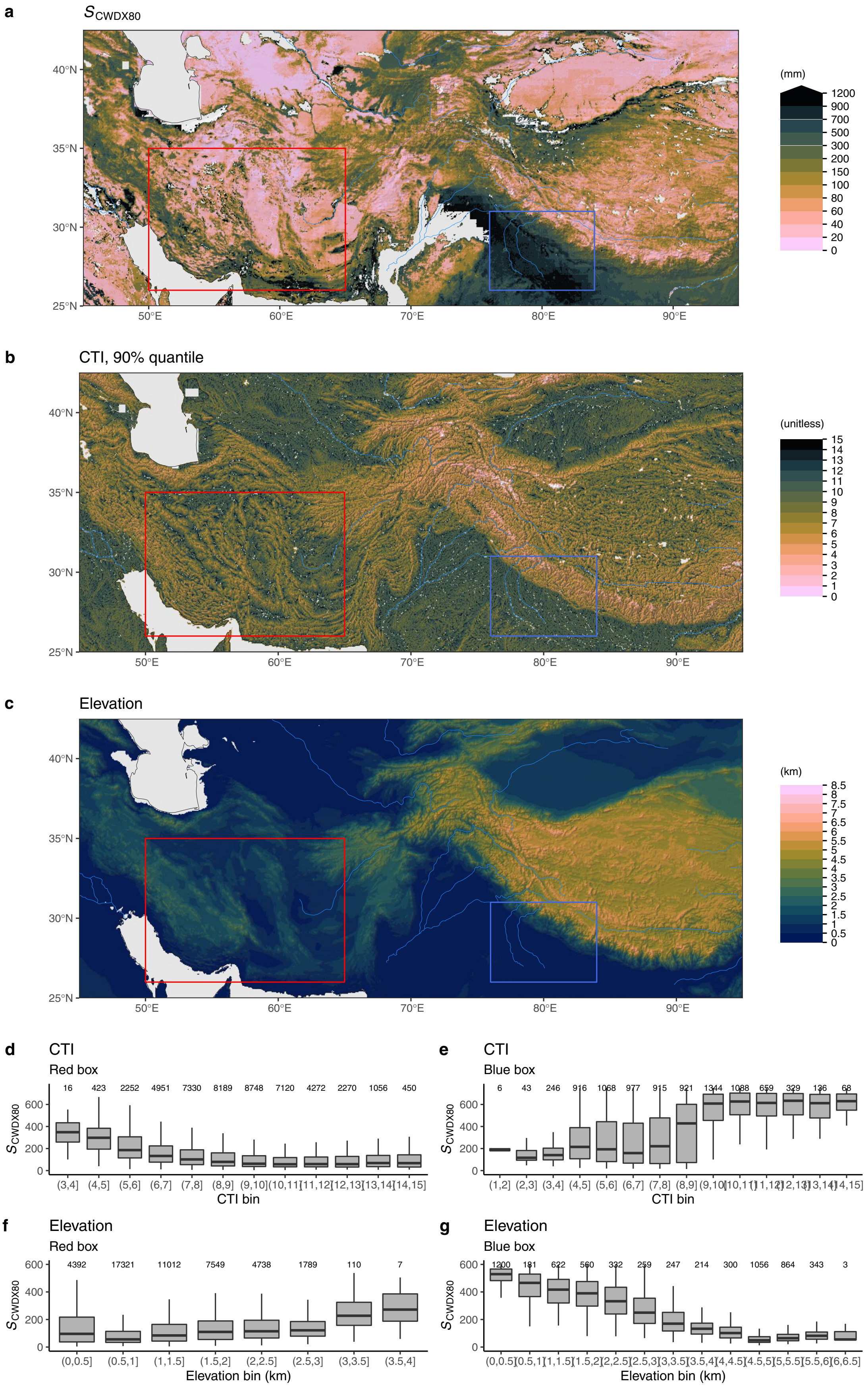

Extended Data Fig. 7 | See next page for caption.

Extended Data Fig. 7 | Rooting zone water storage capacity along topographic gradients in central Asia. (a) Rooting zone water storage capacity in central Asia, estimated by the magnitude of cumulative water deficit extreme events with a return period of 80 years S_{CWDX80}). (b) Compound Topography Index[60], shown as 90% quantiles of underlying pixels, given at 15 arcsec, within matching 0.05° gridcells. (c) Elevation from ETOPO1[43]. Red and blue rectangles indicate the domains for which S_{CWDX80} distributions along a CTI and an elevation gradient are shown in (d), (e), (f) and (g). The Compound Topography Index (CTI) is a measure for subsurface flow convergence and the water table depth based on the topographical setting[61]. Boxes represent the interquartile ranges of binned values (Q_{25}, Q_{75}), and whiskers cover $Q_{25} - 1.5(Q_{75} - Q_{25})$ to $Q_{75} + 1.5(Q_{75} - Q_{25})$. Numbers of data points per bin are given above boxes.

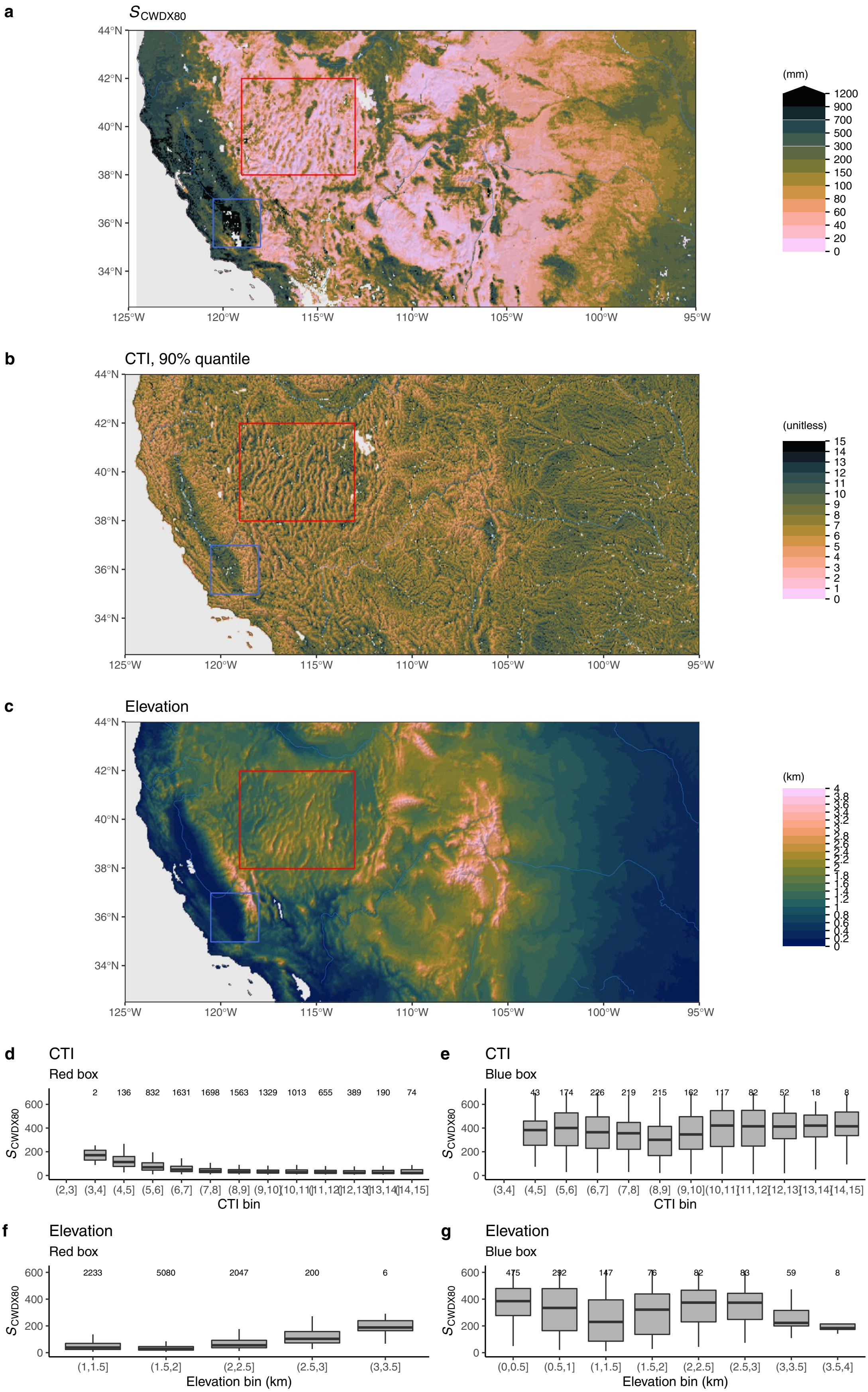

Extended Data Fig. 8 | See next page for caption.

Extended Data Fig. 8 | Rooting zone water storage capacity along topographic gradients in the western United States. (a) Rooting zone water storage capacity in the western United States, estimated by the magnitude of cumulative water deficit extreme events with a return period of 80 years S_{CWDX80}). (b) Compound Topography Index[60], shown as 90% quantiles of underlying pixels, given at 15 arcsec, within matching 0.05° gridcells. (c) Elevation from ETOPO1[43]. Red and blue rectangles indicate the domains for which S_{CWDX80} distributions along a CTI and an elevation gradient are shown in (d), (e), (f), and (g). The Compound Topography Index (CTI) is a measure for subsurface flow convergence and the water table depth based on the topographical setting[61]. Boxes represent the interquartile ranges of binned values (Q_{25}, Q_{75}), and whiskers cover $Q_{25} - 1.5(Q_{75} - Q_{25})$ to $Q_{75} + 1.5(Q_{75} - Q_{25})$. Numbers of data points per bin are given above boxes.